Theoretical and Applied Fracture Mechanics 108 (2020) 102676

Contents lists available at ScienceDirect

Theoretical and Applied Fracture Mechanics

journal homepage: www.elsevier.com/locate/tafmec

Numerical simulation of fatigue crack growth based on accumulated plastic strain

M.F. Borges*, D.M. Neto, F.V. Antunes

Univ Coimbra, Centre for Mechanical Engineering, Materials and Processes (CEMMPRE), Department of Mechanical Engineering, Portugal

ARTICLE INFO

Keywords:
Fatigue crack growth
Finite element method (FEM)
Accumulated plastic strain
Damage accumulation model

ABSTRACT

Fatigue crack growth (FCG) is simulated here by node release, which is made when the accumulated plastic strain reaches a critical value. The numerical procedure is very robust, showing a very fast stabilization and independence relatively to the load considered for node release. A critical accumulated plastic strain of 110% was obtained for the 2024-T351 aluminium alloy, comparing the experimental value of da/dN for a crack length of 26.5 mm and a stress ratio of 0.1, with plane strain numerical predictions. This critical value was used to predict da/dN for different crack lengths. The da/dN-ΔK curve was found to be linear in log-log plot with a slope m = 2.4, which is lower than the slope m = 3.6 presented by the experimental results. The difference is attributed to crack tip mechanisms activated at relatively high loads. The variation of stress ratio and stress state did not affect the da/dN-ΔK curves, which indicates that the effect of these parameters is not linked to crack tip plastic deformation. FCG rate was also predicted for the 7050-T6 aluminium alloy and the 18Ni300 maraging steel, and slopes m = 3.09 and 2.70, respectively, were obtained for da/dN-ΔK curves. The predictions obtained for the steel agreed well with experimental results.

1. Introduction

Fatigue crack growth (FCG) is usually studied experimentally, using CT or MT specimens and assuming that ΔK is the crack driving force [1,2]. ΔK is very convenient because it quantifies the magnitude of crack tip fields, including the effect of crack length, remote stress and specimen geometry. However, the da/dN-ΔK models cannot be used to predict the effect of stress ratio or variable amplitude loading. Besides, they do not provide an understanding of the underlying mechanisms. In fact, the great success of K in last decades obscured the fundamental understanding of FCG. Complementary concepts were proposed, namely crack closure phenomenon, partial closure [3] or CJP model [4], but always keeping ΔK as the main parameter. The crack closure concept, in particular, has been widely used to explain the effect of variable amplitude loading, stress ratio, short cracks and specimen thickness, among other aspects [5]. However, the relevance of crack closure has been questioned by several authors [6]. In fact, all these concepts only mitigated the problem without attacking its real source.

The way for a better understanding of FCG is the simulation of crack tip phenomena, which are effectively responsible for crack progression. Crack tip plastic deformation is usually assumed to be the main mechanism, and the cyclic plastic deformation zone may be considered the process zone. Different parameters have been used to quantify crack tip plastic deformation, namely, the plastic strain or the ratchetting strain measured ahead of crack tip, the size of reversed plastic zone, the dissipated energy and the CTOD. Pokluda [7] stated that the crack driving force in fatigue is directly related to the range of cyclic plastic strain. Tong *et al.* [8] used the progressive accumulation of tensile strains, ε_{yy}, occurring near the crack tip to predict FCG rate. Zhang *et al.* [9] correlated the size of reversed plastic zone for the 2024-T351 aluminium alloy with da/dN. Ould Chick *et al.* [10] proposed a linear relation between the square of the cyclic plastic zone size and FCG rate. On the other hand, Zhang and Du [11] proposed that plastic deformation is mainly introduced during the loading part of the load cycle and correlated da/dN with the size of monotonic plastic zone. The crack tip opening displacement (CTOD) is a classical parameter of ductile fracture, which was also applied to FCG. Pelloux [12] linked CTOD with fatigue striations spacing and therefore with FCG rate. Tvergaard [13] and Pippan and Grosinger [14], proposed a linear relation between CTOD and da/dN for ductile materials. Different authors predicted FCG rate simulating alternating crack-tip blunting and resharpening [13,15]. Antunes *et al.* [16] and Vasco-Olmo *et al.* [17,18] assumed that crack tip plastic deformation can be quantified by the plastic CTOD range, and obtained linear relations between da/dN and this plastic CTOD. The relation between the plastic CTOD obtained numerically and the experimental da/dN, was used to predict the effect of Young's

* Corresponding author.
E-mail address: fernando.ventura@dem.uc.pt (M.F. Borges).

https://doi.org/10.1016/j.tafmec.2020.102676
Received 15 April 2020; Received in revised form 12 May 2020; Accepted 11 June 2020
Available online 16 June 2020
0167-8442/

Nomenclature

a_0	Initial crack length
AA	Aluminum Alloy
CT	Crack Tension (specimen)
CTOD	Crack Tip Opening Displacement
$CTOD_p$	Plastic Crack Tip Opening Displacement
C, n, Y_0	Material constants of Swift isotropic hardening law
C_x, X_{Sat}	Material constants of Lemaître-Chaboche kinematic hardening law
da/dN	Fatigue crack growth rate
DIC	Digital Image Correlation
F	Applied force
F_{max}	Maximum applied force
F_{min}	Minimum applied force
FCG	Fatigue Crack Growth
K_{max}	Maximum stress intensity factor
K_{min}	Minimum stress intensity factor
m	Slope
R	Stress ratio
t	Specimen's thickness
W	Specimen's width
Δa	Crack growth
ΔK	Stress intensity factor range (K_{max}-K_{min})
ΔK_{eff}	Effective stress intensity factor range (K_{max}-K_{open})
ΔN	Number of cycles between crack propagation
$\Delta \varepsilon^p$	Accumulated plastic strain
$\Delta \varepsilon_c^p$	Critical value of accumulated plastic strain
$\bar{\sigma}$	Equivalent stress
$\boldsymbol{\sigma}'$	Deviatoric Cauchy stress tensor
$\bar{\varepsilon}^p$	Equivalent plastic strain
$\dot{\bar{\varepsilon}}^p$	Equivalent plastic strain rate
$\boldsymbol{X}$	Back stress tensor

modulus [19], stress ratio, stress state and variable amplitude loading [20]. Other authors suggested that the total plastic dissipation per cycle is a driving force for fatigue crack growth in ductile solids [21]. Bodner *et al.* [22] proposed that FCG rate is proportional to the total plastic dissipation per cycle occurring throughout the reversed plastic zone ahead of the crack tip. Jiang and Feng [23] proposed a damage parameter proportional to the plastic work. They assumed that the crack advances once the fatigue damage accumulation reaches a certain critical value and developed a relationship for the crack growth rate in terms of the damage per cycle ahead of the crack tip. Susmel [24] proposed the theory of critical distances. The accumulated plastic energy density at the critical point ahead of crack tip is used as a measure of the fatigue damage. The damage condition at the critical point is assumed to represent the average damage condition at the crack tip. Hosseini *et al.* [25] released the crack-tip node when the accumulated plastic work density at the crack-tip element reached a critical value.

The objective here is the finite element simulation of FCG using a damage accumulation approach based on cumulative plastic strain measured immediately ahead of crack tip. The plastic strain at crack tip is the most immediate parameter, assuming that FCG is linked to plastic deformation. The propagation is defined by nodal release, therefore is discrete, which justifies the need of a cumulative strain. Comparatively to our previous works based on CTOD [16–20]: (i) there is a movement from behind to ahead of crack tip; (ii) only one experimental value is considered to calibrate the critical plastic strain, while several points were used to calibrate the da/dN versus plastic CTOD law.

2. Numerical model

The numerical simulations of the fatigue crack growth were carried out with the in-house static implicit finite element code DD3IMP [26], which was specifically developed to simulate sheet metal forming processes [27]. The incremental nonlinear analysis is defined by an updated Lagrangian formulation. The mechanical model considers the elasto-plastic behavior of the deformable body (CT specimen), where the elastic behavior is assumed isotropic while the plastic behavior can be considered anisotropic. The frictional contact problem is regularized by the augmented Lagrangian method [28], using the node-to-surface to discretize the contact interface. In each increment, the non-linearities associated with the elastoplastic behavior and the contact problem are solved simultaneously by an implicit Newton–Raphson scheme, using an explicit approach to calculate the required trial solution.

The geometry and main dimensions of the CT specimen adopted in the present study are presented in Fig. 1. Considering the symmetry relatively to the plane of the crack, only the upper part of the CT specimen was simulated, as illustrated in Fig. 2a. Accordingly, the potential contact of the crack flanks is modeled considering a fixed flat surface in the symmetry plane. Since the sliding between the crack surfaces is null, frictionless contact conditions are assumed on the flat surface to avoid the generation of frictional forces. This rigid surface prevents the overlapping of crack surfaces during unloading. Since the pins were not modelled, the cyclic load is applied in the upper point of the specimen hole, which allows the rotation between the pins and holes of the specimen according to experimental conditions. Besides, the displacement of that point is constrained in the x-direction, avoiding the rigid body motion of the specimen. A small thickness of 0.1 mm was considered in the numerical models, to reduce the numerical effort. Both plane stress and plane strain conditions were considered in the study, considering adequate out-of-plane boundary conditions as illustrated in Fig. 2d and e.

A set of tests was considered with different load ratios. Table 1 presents the loads considered for the different stress ratios, R, which were defined according previous experimental work [29]. a_{min} and a_{max} represent the minimum and maximum crack lengths, respectively, measured in the experimental work, while F_{min} and F_{max} indicate the maximum and minimum loads, respectively, applied in the numerical models. Since the experimental work used specimens with a thickness of 12 mm, the loads presented in Table 1 were obtained from the experimental values dividing by 120.

The specimen geometry (upper half part) was discretized with 8-node hexahedral finite elements, using a selective reduced integration technique [30] to avoid volumetric locking. In order to reduce the

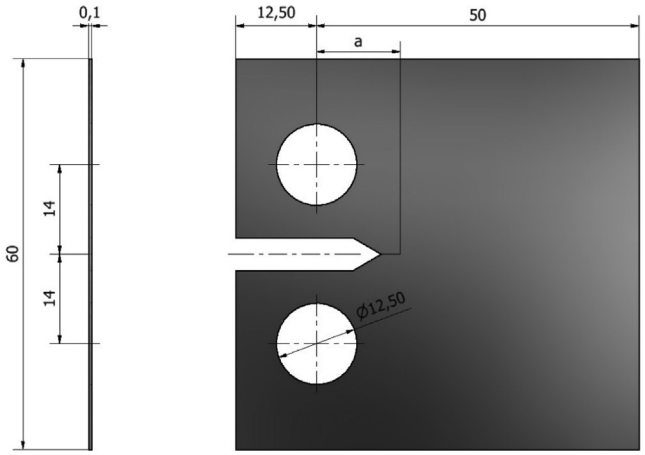

Fig. 1. Compact Tension simulated numerically, for AA2024-T351, with dimensions in mm.

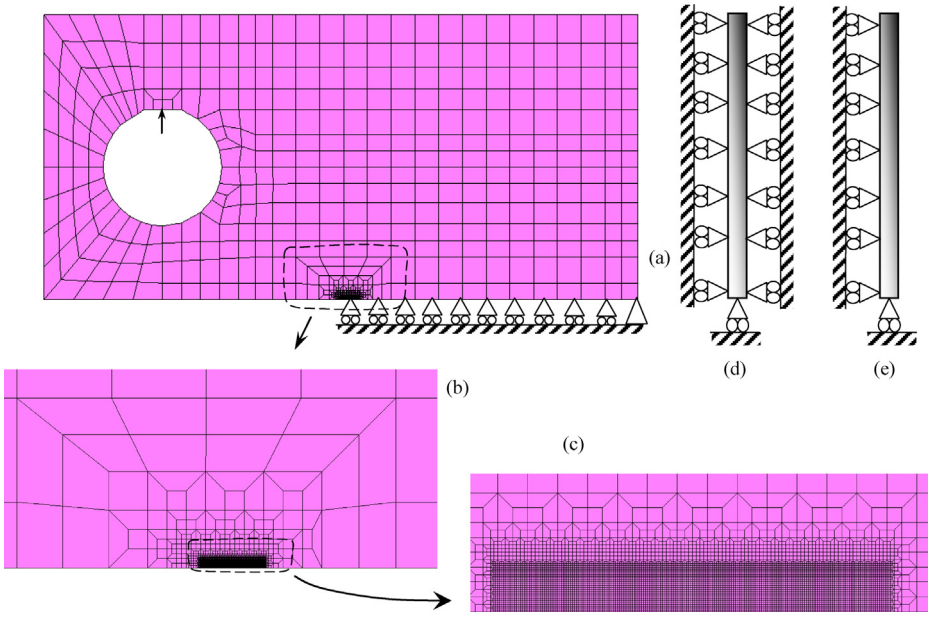

Fig. 2. Model of the C(T) specimen. a(a) Load and boundary conditions. (b) (c) Details of finite element mesh. (d) Plane strain boundary conditions. (e) Plane stress boundary conditions.

Table 1
Load parameters.

R	a_{min} [mm]	a_{max} [mm]	F_{min} [N]	F_{max} [N]
0.1	12	30	4.17	41.67
0.3	12	29	14.00	46.67
0.5	12	26.7	35.42	70.83
0.7	12	22.5	72.92	104.17

computational cost of the numerical simulations, only the region near the crack growth path is uniformly meshed with finer elements of 8 μm, as Fig. 2 illustrates. This element size allows the accurate evaluation of the strong gradients of stresses and strains near the crack tip. Only a single layer of elements was used in the thickness direction.

2.1. Elasto-plastic behaviour

The material studied was the 2024-T351 aluminium alloy plate. The main material properties are presented in Table 2. An elastic-plastic model was used considering Hooke's law to describe the isotropic elastic behavior, von Mises yield criterion and a Swift isotropic hardening law coupled with Lemaître-Chaboche kinematic hardening law, Eqs. (1) and (2) respectively, under an associated flow rule, to describe the isotropic plastic behaviour.

$$Y = C\left[\left(\frac{Y_0}{C}\right)^{\frac{1}{n}} + \bar{\varepsilon}^p\right]^n, \tag{1}$$

where Y is the flow stress, Y_0, C and n are the material parameters of Swift law and $\bar{\varepsilon}^p$ is the equivalent plastic strain.

$$\dot{\boldsymbol{X}} = C_X\left[X_{Sat}\frac{\sigma' - \boldsymbol{X}}{\bar{\sigma}} - \boldsymbol{X}\right]\dot{\bar{\varepsilon}}^p, \tag{2}$$

where $\boldsymbol{\sigma'}$ is the deviatoric Cauchy stress tensor, $\boldsymbol{X}$ is the back stress tensor, $\bar{\sigma}$ is the equivalent stress and $\dot{\bar{\varepsilon}}^p$ is the equivalent plastic strain rate, C_X and X_{Sat} are the material parameters of Lemaître-Chaboche law. Table 3 presents the identified set of material parameters.

2.2. Fatigue crack growth algorithm

Considering the geometry of the CT specimen and the applied loading, the crack path arises in the symmetry plane, which extends over the entire specimen thickness. In order to simulate the continuous advance of the crack tip, the nodes over the crack path are released according to the proposed algorithm. However, the discretization of the crack path with finite elements leads to a discontinuous crack growth, i.e., the crack increment is dictated by the finite element size (8 μm).

Since the fatigue crack growth is mainly driven by the plastic deformation around the crack tip, the proposed algorithm is based on plastic strain value. Due to the singularity induced by the geometrical discontinuity of the crack, the equivalent plastic strain is measured at the two Gauss points around the crack tip node (immediately behind and ahead), using the average to define plastic strain value at the crack tip. Accordingly, the crack tip node is released when the plastic strain reaches a critical value, using the instant of maximum or minimum load to perform the comparison and consequent release. The critical plastic strain for node release is supposed to be a material property. After each crack node release, the accumulated plastic strain is set to zero, and its accumulation is quantified with the application of the cyclic load. This means that the plastic deformation that occurred before at those Gauss points is ignored in the proposed fatigue crack growth algorithm. Anyway, this previous deformation is supposed to affect material hardening.

The predicted FCG rate is obtained from the ratio between the crack increment (8 μm) and the number of load cycles ΔN required to reach the critical value of plastic strain. Hence, the FCG rate is assumed constant between crack increments. Since the crack propagation rate is usually relatively low (< 1 μm/cycle), the numerical analysis of the crack growth is simplified by considering different sizes for the initial straight crack. The continuous advance of the crack tip is appropriately replaced by a set of small crack propagations (< 500 μm), distributed

Table 2
Mechanical properties of 2024-T351 aluminium alloy.

Young modulus	Yield Stress	UTS	Elongation at Break	Brinell Hardness
73 GPa	325 MPa	470 MPa	20%	137

Table 3
Swift and Lemaître-Chaboche laws parameters for the 2024-T351 aluminium alloy.

Material	Y_0 [MPa]	C [MPa]	n	C_x	X_{Sat} [MPa]
2024-T351	288.96	389.00	0.056	138.80	111.84

over the crack path, specifically for the initial crack sizes, a_0, of 5, 9, 11.5, 14, 16.5, 19, 21.5, 24, and 26.5 mm. Some crack propagation is required to stabilize the cyclic plastic deformation and the crack closure level. Only after that the FCG parameters are evaluated, namely the crack growth rate.

3. Numerical results

3.1. Crack tip plastic strain versus cyclic loading

Fig. 3a presents both the evolution of plastic strain, ε^P, measured at the crack tip and the applied force, F, as a function of the pseudo-time. These results were obtained under plane strain conditions, for a stress ratio R = 0.1, an initial crack length a_0 = 21.5 mm, after a crack growth, Δa, of 0.144 mm, and assuming an arbitrary critical value of increment plastic strain $\Delta\varepsilon_c^P$ = 110%. Since the material is assumed strain rate insensitive, the time is not a variable of the problem. Thus, it is presented only for visualization purposes, where each load cycle has a duration of 2 s (loading + unloading) and a triangular shape. For simplification reasons, the zero of time was assigned to the beginning of the last load cycle before the nodal crack propagation. When the crack increment occurs, the tip goes to the next node and, therefore, $\Delta\varepsilon^P$ is evaluated at this new node. This is the reason why there is sudden decrease of ε^P in Fig. 3a. After that, $\Delta\varepsilon^P$ increases progressively with cyclic loading until achieve the critical accumulated plastic strain, $\Delta\varepsilon_c^P$, defined at the beginning of the numerical simulation. Under these conditions, 19 load cycles were needed to reach the critical strain, therefore the average crack growth rate in Fig. 3a is da/dN = 8/19 = 0.42 μm/cycle.

In order to highlight the relationship between the applied loading cycles and the generated plastic strain in the crack tip, Fig. 3b shows the evolution of $\Delta\varepsilon^P$ during two load cycles. When the specimen is loaded, first the crack tip experiences elastic deformation, i.e. $\Delta\varepsilon^P$ remains constant between points *A* and *B*. Then, $\Delta\varepsilon^P$ rapidly increases by increasing *F* until this reaches its maximum value, F_{max}, at point *C*. The same behaviour is verified during the unloading of the specimen, where $\Delta\varepsilon^P$ remains unchanged during the elastic regime (path C-D). For lower values of *F*, reversed plastic deformation occurs at the crack tip, due to local compressive loads. Since the crack driving force is assumed to be the accumulated plastic strain, there is an increase of plastic strain even during unloading. The accumulation of plastic strain during unloading is slightly lower than that observed during loading. Point *E* corresponds to the minimum applied load, F_{min}.

Fig. 4a and b show the CTOD and plastic CTOD, $CTOD_p$, respectively for a particular load cycle. It should be noted that the points (A-E) presented in Figs. 3b, 4a and b were obtained in the same instant of simulation, giving an interesting link between what happens at the crack tip, quantified by ε^P, and behind the crack tip, measured by CTOD and $CTOD_p$. CTOD was measured at the first node behind the crack tip, i.e., at a distance of 8 μm from the crack tip. Fig. 4a presents the total CTOD, which is the sum of the elastic and plastic values. Between *A* and *B* there is only elastic deformation, and after point *B* there is a departure from the linearity. The elastic and plastic CTOD ranges corresponding to the loading portion of the cycle are represented. Increasing the distance between the crack tip and the point of measurement increases the elastic CTOD and decreases the plastic CTOD. The evolution of $CTOD_p$ presented in Fig. 4b is in agreement with the evolution observed for ε^P (see Fig. 3b), showing two regions without plastic deformation (A-B and C-D) and two regions with a progressive increase of plasticity (B-C and D-E). The rate of variation of plastic CTOD increases progressively with load. The range of plastic deformation during unloading is slightly lower than during loading, exactly as was observed for the plastic strain. This similarity indicates that different parameters can be used to quantify crack tip plastic deformation. Note that the plastic CTOD has positive and negative variations, generating a loop, while the plastic strain in the crack tip is a cumulative value, i.e., it is always increasing even during unloading. Similar trends were found for plane stress state.

Regarding the computational cost of the finite element simulations, it is strongly dependent from the adopted finite element mesh. Although a wide range of the initial crack size has been used, all models comprises about 7300 finite elements and approximately 15,000 nodes. Considering the application of 350 loading cycles, the computational time is approximately 16 h and 24 h considering plane strain and plane stress conditions, respectively. Since the number of degrees of freedom in the model considering plane stress conditions is 25% larger than in the model under plane strain conditions, the computational cost increases 50%. All simulations were performed on a computer machine equipped with an Intel ®Core TM i7-950 Quad-Core processor (3.07 GHz).

3.2. Transient effect

The analysis of the crack growth considered different sizes for the initial crack length and transient effects are observed at the beginning of each numerical simulation. They are associated with the stabilization of cyclic plastic deformation and the formation of residual plastic wake, which may produce crack closure. Fig. 5a–d show the stabilization of da/dN with crack increment, Δa, for a_o = 9 mm and a_o = 26.5 mm, comparing plane stress and plane strain conditions for arbitrary values of accumulated plastic strain, $\Delta\varepsilon_p$. Considering plane strain conditions, da/dN stabilizes more quickly (i.e., for lower values of Δa) than in plane

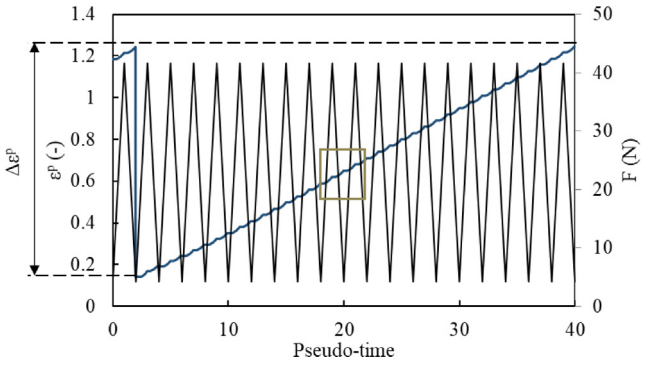

(a)

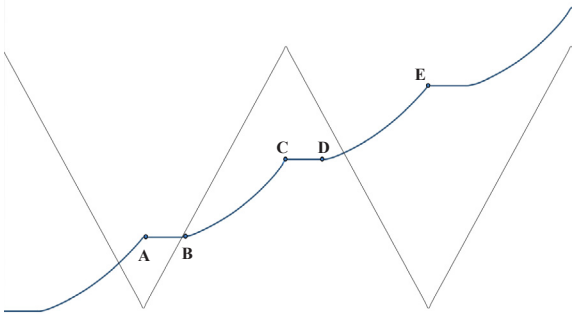

(b)

Fig. 3. (a) Evolution of ε^P and F, with pseudo-time; (b) Detail of the behavior of ε^P, and F, with time (Plane Strain; $\Delta\varepsilon^P$ = 110%, R = 0.1 and a_o = 21.5 mm).

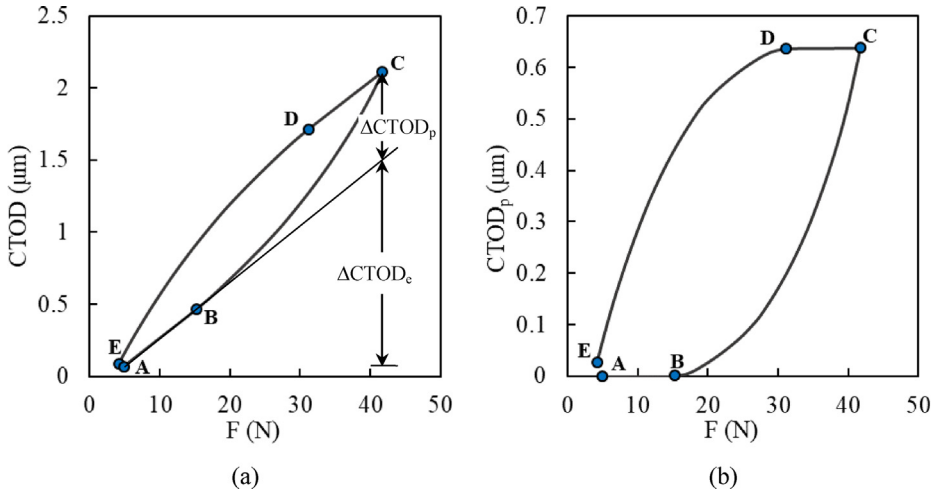

Fig. 4. Evolution of CTOD vs. F curves, between propagations, in stable *da/dN* values, for a_o = 26.5 mm, R = 0.1, $\Delta\varepsilon^p$ = 110%; plane strain state.

stress conditions. Moreover, increasing the initial size of the crack, *da/dN* stabilizes for longer values of *Δa*. For plane stress conditions and a_o = 26.5 mm, Fig. 5d, a relatively large propagation is required to stabilize da/dN, which is the contrast to plane strain conditions and a_o = 9 mm. After stabilization there is a progressive increase of da/dN with crack growth, as is evident in Fig. 5c, which is due to the progressive strengthening of crack tip singularity. The minimum values in Fig. 5a and c correspond to the end of transient regime.

The effect of the critical value of plastic strain, $\Delta\varepsilon_c^p$, can also be seen in these figures. The increase of $\Delta\varepsilon_c^p$ dictates that more load cycles are required to reach the critical strain, which reduces *da/dN*. Thus, considering a fixed number of load cycles, the total crack increment is smaller for larger values of $\Delta\varepsilon_c^p$. Besides, since the crack growth rate is significantly higher for large values of a_0, considering the same number

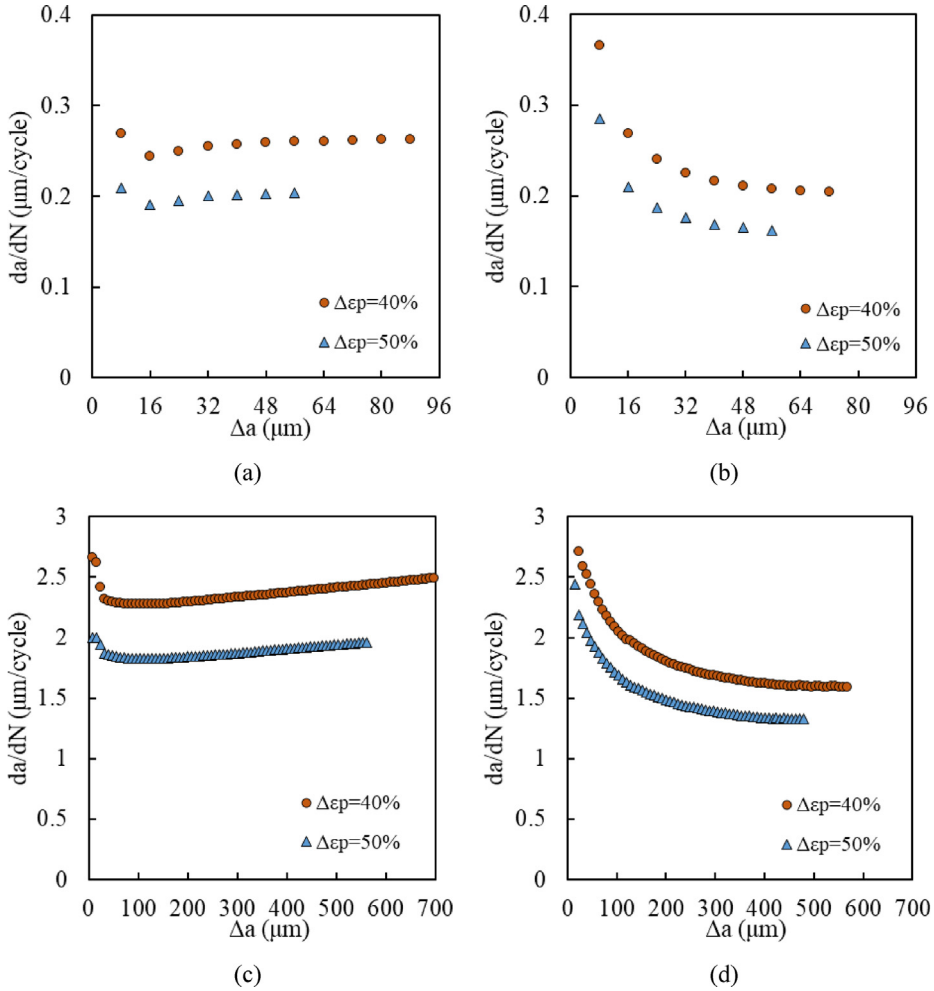

Fig. 5. Stabilization of *da/dN* with *Δa*. (a) a_o = 9 mm, plane strain; (b) a_o = 9 mm, plane stress; (c) a_o = 26.5 mm, plane strain; (d) a_o = 26.5 mm, plane stress, $\Delta\varepsilon_c^p$ = 40% (circular marker) and $\Delta\varepsilon_c^p$ = 50% (triangular marker).

of load cycles the crack increment is bigger for large values of a_0, as shown in Fig. 5a and 5c. On the other hand, the value of $\Delta\varepsilon_c^p$ does not seem to affect the distance of stabilization of FCG rate. All *da/dN* values presented next were evaluated in stable zones.

3.3. Critical value of plastic strain

Assuming that plastic strain is the crack driving force, the numerical prediction of FCG rate was based on the crack tip plastic strain. A comparison between numerical and experimental FCG rates, for the same a_0 and *R*, was made to find a critical value of $\Delta\varepsilon^p$, which is supposed to be a material property. This comparison was aimed at the highest value of a_0, namely at a_0 = 26.5 mm, to reduce the eventual interference of oxidation. In fact, for relatively small crack lengths, the FCG rate is small therefore the environmental mechanisms have time to actuate and compete with cyclic plastic deformation as crack driving force.

Different values of $\Delta\varepsilon_c^p$, were adopted in the numerical simulations, allowing to predict different values of *da/dN*. Fig. 6 plots the predicted *da/dN* versus selected $\Delta\varepsilon_c^p$, for R = 0.1 in plane strain conditions. The increase of $\Delta\varepsilon_c^p$ reduces *da/dN*, since more load cycles are needed to reach the critical accumulated strain. This trend was previously observed in Fig. 5. The experimental value of *da/dN* was obtained in literature [29]. The CT specimen used in the experimental work had a relatively large thickness of 12 mm, which explains the option for plane strain conditions in the numerical analysis. For thicknesses greater than or equal to 10 mm, a plane strain state is usually assumed [31]. A non-linear interpolation enables the extraction of the critical value of $\Delta\varepsilon_c^p$ that gives a numerical *da/dN* equal to the experimental one. A critical $\Delta\varepsilon^p$ of 110% was obtained, as can be seen in Fig. 6. Tong *et al.* [8] used the accumulation of the strain component normal to the crack growth plane at a characteristic distance to the crack tip (12.7 μm) to simulate FCG. Also using one experimental value of da/dN, they found an accumulative plastic strain of 57% for a nickel-based superalloy.

3.4. Effect of crack length

Fig. 7 plots ε^p versus pseudo-time for the first two load cycles after the last crack propagation, for simulations with a_0 equal to 5, 19 and 26.5 mm. The zero of pseudo-time was matched with the instant where the crack propagation occurred, for each simulation. The initial values of ε^p are higher for larger values of a_0, as highlighted by the arrows in Fig. 7. This may be attributed to the higher size of the plastic zone, which is linked to a_0, placing the node well inside the plastic zone for a_0 = 26.5 mm. Besides, the evolution of ε^p, due to the effect of loading, is more pronounced for higher values of a_0. This could be expected considering that the increase of crack length increases the magnitude of crack tip stress fields.

After defining the critical value of accumulated plastic strain, $\Delta\varepsilon_c^p$, simulations with different values of a_0 were performed to compare the predicted crack growth rate with experimental results [29]. The comparison between experimental and numerical ($\Delta\varepsilon_c^p$ = 110%) *da/dN-ΔK* curves for R = 0.1 are presented in Fig. 8a and b, in linear and logarithmic scales, respectively. The numerical curve is a straight line in log-log graph, with a slope of m = 2.4, while the experimental results have m = 3.6. Zheng *et al.* [32] also obtained predicted slopes lower than the experimental values. The slope of 2 is typical in numerical simulations which assume the plastic strain as crack driving force, while a slope of 4 is obtained with approaches based on dissipated energy [25]. The values of *m* obtained experimentally are usually in the range 2–4.

The experimental and numerical results are coincident for a_0 = 26.5 mm, since this crack length was used to define the critical value of acumulated plastic strain. However, the numerical curve is above the experimental one for small crack lengths. This difference leads to the assumption that other mechanisms may affect FCG, in addition, to crack tip plastic deformation. The oxidation is expected to be more relevant at relatively low crack growth rates, but this would put the experimental curve above the numerical predictions, which is not the case. Therefore, the difference needs to be linked to mechanisms which are active at relatively high loads, like coalescence of microvoids or brittle mechanisms controlled by K_{max}. Kujawski [33] proposed a driving force which is a function of K_{max} and ΔK^+, the positive range of ΔK: $\Delta K_{eff} = (K_{max})^{\alpha}(\Delta K^+)^{1-\alpha}$. The α parameter quantifies the sensitivity to the applied K_{max} value. Values of 0.3, 0.33, 0.5, 0.5, 0.6 were obtained for medium carbon steel, Udimet 720 nickel base superallloy, AA7075-T6, AA2024-T351 and austempered ductile iron, respectively. According Kujawski, materials which usually are assumed to have a ductile behaviour, are partially brittle. Llanes *et al.* [34] studied FCG in WC-Co cemented carbides and observed a prevalence of K_{max} over ΔK as the controlling parameter, which was attributed to the predominance of static failure modes. They proposed a modification of Paris-Erdogan relationship of the form: $da/dN = C(K_{max})^n(\Delta K)^m$, where the values of *m* and *n* define the relative dominance of each parameter. Pippan *et al.* [35] indicated a strong effect of K_{max} on the fatigue crack propagation rate of brittle materials. The identification and quantification of the brittle or ductile mechanisms activated by K_{max} is of major importance to understand FCG.

3.5. Effect of stress ratio

A parametric study was carried out to quantify the effect of stress ratio on the predicted crack growth rate. The predicted *da/dN-ΔK* curves obtained with $\Delta\varepsilon_c^p$ = 110% for *R* equal to 0.1, 0.3, 0.5 and 0.7 are presented in Fig. 9a and b in linear and logarithmic scales, respectively, which are compared with experimental curves for *R* equal to 0.1 and 0.7 [29]. Regarding the numerical results, there is almost no effect of R on *da/dN-ΔK* relations. On the other hand, in experimental results the effect of R on FCG rate is evident, which is usually linked to crack closure phenomenon. Thus, the absence of effect of *R* in numerical results seems to be connected to the absence of crack closure, as evidenced in CTOD vs. F curve in Fig. 4a. Besides, it indicates that crack tip plastic deformation is not directly responsible for the effect of stress ratio. Since the CT specimens were relatively thick, the plane strain state is dominant and therefore a limited effect of crack closure may be expected. Therefore, the effect of stress ratio may be associated with K_{max} dependent mechanisms. Alternatively, the experimental results may indicate that plane strain state is not so dominant as is being assumed.

3.6. Effect of stress state

To evaluate the effect of stress state on FCG rate, plane stress cases

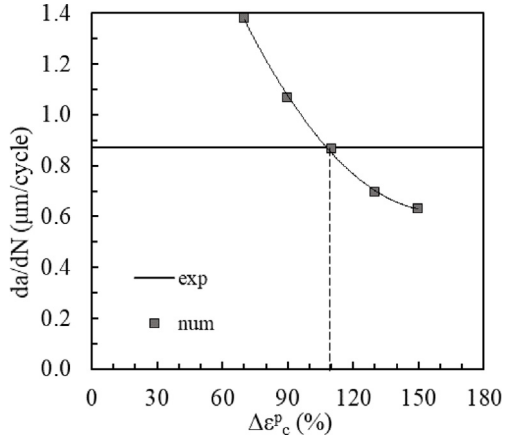

Fig. 6. Extraction of $\Delta\varepsilon_c^p$ for a_0 = 26.5 mm, R = 0.1 and plane strain state.

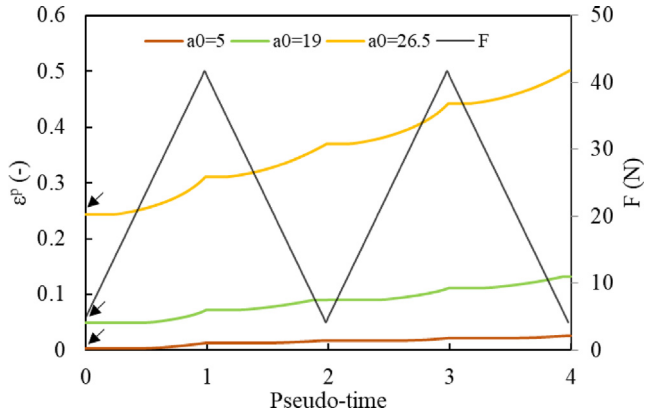

Fig. 7. Evolution of ε^P with pseudo-time, for the first two load cycles after the last propagation, R = 0.1, $\Delta\varepsilon^P$ = 40%, and plane strain state.

were also studied. First, a new critical value of $\Delta\varepsilon^P$ was defined, similarly as performed in plane strain, by running various simulations for a_0 = 26.5 mm and comparing the FCG rate obtained numerically with the experimental value [29], as shown in Fig. 10 that plots the predicted *da/dN* versus $\Delta\varepsilon_c^p$. A critical value of $\Delta\varepsilon^P$ equal to 83% was obtained by interpolating $\Delta\varepsilon_c^p$ equal to 80% and 90%. The critical value of $\Delta\varepsilon^P$ in plane stress is lower than in plane strain, which indicates that less accumulated plastic strain, $\Delta\varepsilon^P$, is required in plane stress conditions to obtain the same FCG rate. Since the critical cumulative plastic strain is expected to be a material property, only one value must exist for each material. This second value of $\Delta\varepsilon_c^p$ is not proposed to have the strength of a material law, being defined only to adjust the position of the da/dN-ΔK curve.

The comparison between predicted and experimental *da/dN* against ΔK for R = 0.1 is presented in Fig. 11a and b, in linear and logarithmic scales, respectively. The experimental and numerical curves in plane strain and plane stress are coincident for a_0 = 26.5 mm, which is a consequence of the procedure followed to obtain the critical accumulated strain as illustrated in Figs. 6 and 10. The subscripts *Fmin* and *Fmax* indicate that the node release occurs at the instant of minimum and maximum loads, respectively, while the subscript *no_contact* indicates that the contact of crack flanks was removed from the model in order to eliminate the crack closure phenomenon. In all the other series the contact of crack flanks is possible, allowing the simulation of plasticity induced crack closure. The effect of stress state on predicted FCG rate is small. Anyway, for short cracks, the FCG rate is slightly higher for plane stress state than for the plane strain state. In plane stress cases, a comparison is made with and without contact at the crack flanks. Without contact, crack closure phenomenon is disabled, which permits the analysis of FCG without the interference of this phenomenon. In these simulations, higher FCG rates are achieved for the same geometrical and loading parameters. This aspect comes from the higher effective loads, and therefore higher effective stress intensity factor ranges ΔK_{eff}, contributing to higher plastic deformation. $\Delta\varepsilon_c^p$ is reached more quickly since less ΔN is needed, which leads to higher FCG rates. These results indicate that plasticity induced crack closure is relevant under plane stress conditions for the 2024-T351 aluminium alloy. It was also made a study about crack propagation occurring at minimum and maximum load in plane strain conditions. Fig. 11a and 11b show no effect of this numerical parameter in the predicted FCG rate, which is a good indication for the robustness of the numerical approach.

4. Discussion

In order to check if the slope of *da/dN-ΔK* curves predicted numerically and the positioning relatively to experimental results are always the same, another two materials were studied. The first material selected was the 7050-T6 aluminium alloy [16]. This study was focused on the effect of the material on *da/dN-ΔK* curves and therefore the geometry was the same, as well as the critical $\Delta\varepsilon^P$ = 110%, plane strain state and loading conditions conducting to R = 0.1 (see table 1). Note that the critical accumulated strain is expected to change with material, however, the value assumed for the AA7050-T6 was that obtained for the AA2024-T351, because the objective was just to study the slope of da/dN-ΔK curves. Table 4 presents the parameters of the elastic-plastic model considered for this material while Fig. 12 presents the predictions obtained. The change of material parameters produced a significant increase of the slope of da/dN-ΔK curves, indicating a significant impact of elastic-plastic behaviour on FCG rate.

The second material considered for comparison was the 18Ni300 steel, in the form of CT specimen with W = 36 mm, as schematized in Fig. 13. The set of elastic-plastic parameters identified for this material is presented in Table 4 [36]. Only plane strain state and a thickness t = 0.1 mm were assumed in the numerical models. The specimen was submitted to a cyclic load with magnitudes of 2.48 N and 49.61 N, therefore, *R* is equal to 0.05. Since the thickness of the CT specimens used in the experimental work was 3 mm, the loads applied in the numerical models were obtained from the experimental values dividing by 30. Several values of a_0 were simulated concretely 7, 10, 13, 16, 19, 22 and 24 mm. The same mesh refinement was employed at the crack tip region, with elements with 8 × 8 μm^2. The reasoning followed in the study of the AA2024-T351 was adopted for the 18Ni300 steel. First,

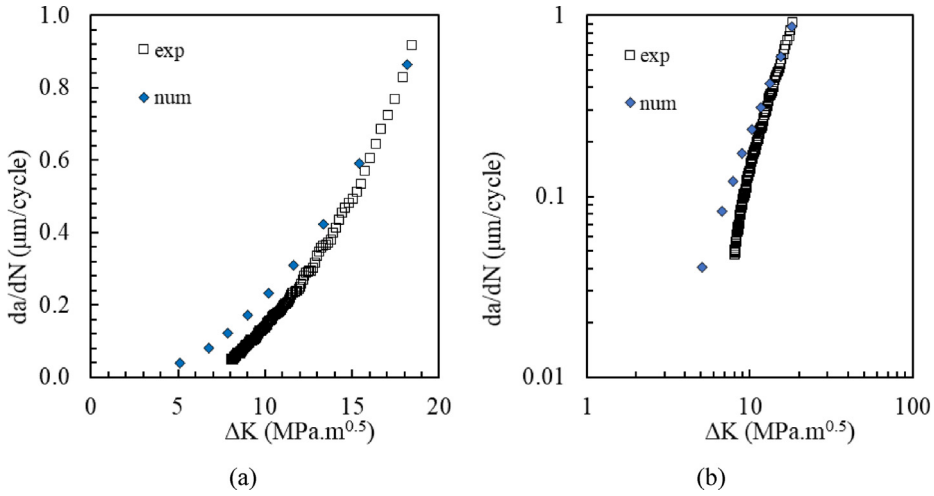

Fig. 8. *da/dN* versus ΔK curves, in plane strain conditions and with R = 0.1: (a) linear scales; (b) logarithmic scales.

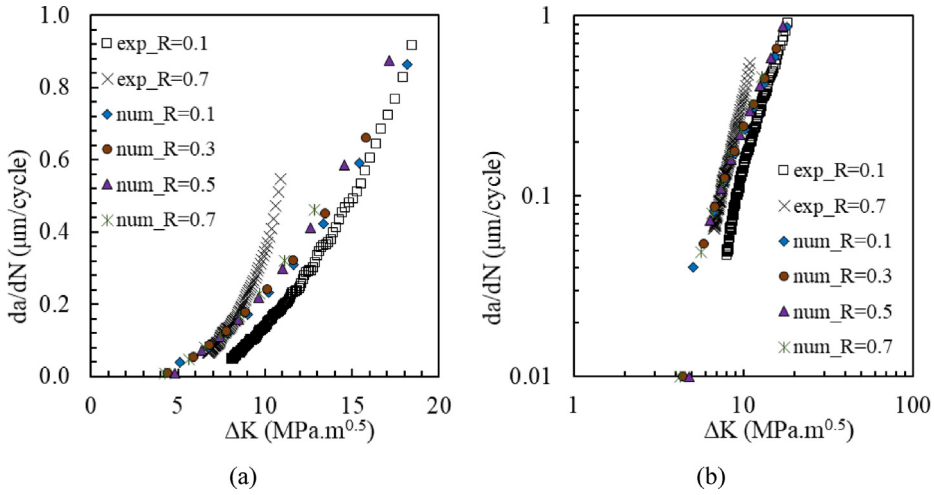

Fig. 9. Effect of stress ratio in *da/dN* versus *ΔK* curves, in plane strain conditions: (a) linear scales; (b) logarithmic scales.

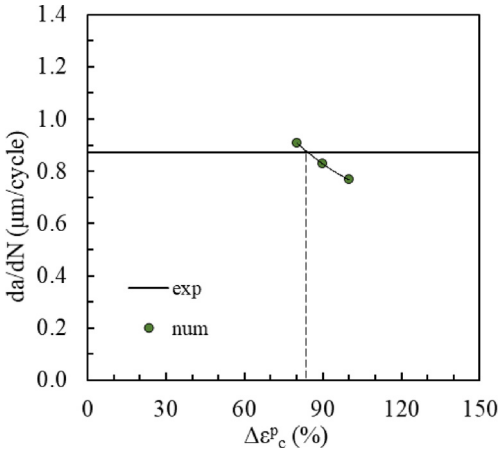

Fig. 10. Extraction of $\Delta\varepsilon_c^p$ for a_0 = 26.5 mm, R = 0.1 and plane stress state.

a set of simulations for a_0 = 24 mm was performed with different values of $\Delta\varepsilon_c^p$. The results were analysed and the FCG rate was calculated and compared with the experimental data for the same crack length. A linear interpolation was made and the value of $\Delta\varepsilon_c^p$ = 78.6% was extracted, resulting in a numerical FCG rate equal to the experimental, as shown in Fig. 14. The numerical tests were then conducted with

Table 4
Parameters of Swift isotropic and Lemaître-Chaboche kinematic hardening laws.

Material	E [MPa]	ν [–]	Y_0 [MPa]	C [MPa]	n [–]	C_x [–]	X_{Sat} [MPa]
AA7050-T6	71.7	0.3	420.50	420.50	0	228.91	198.35
18Ni300	160	0.33	683.62	683.62	0	728.34	402.06

$\Delta\varepsilon^p$ = 78.6% to compare with the experimental results. The comparison between experimental and numerical *da/dN* against *ΔK* is presented in Fig. 15a and b that are in linear and logarithmic scales, respectively. The numerical results are in good agreement with the experimental data. Even for lower values of a_0, the numerical curve is overlapped with the experimental one, in opposite to the results of the AA2024-T351. Some difference between the curves is observed for intermediate values of a_0. The slopes of both numerical and experimental curves were retrieved from Fig. 15b, conducting to m = 2.7 for the numerical and m = 2.9 for the experimental results. Therefore, for the materials studied here the slopes predicted numerically are of the same order, ranging from 2.4 to 3.1. In this case, the numerical results show a slope similar to the experimental, which results in the almost superposition of the curves. Antunes *et al.* [36] observed that this material showed a very limited effect of stress ratio and specimen thickness on FCG rate, which was attributed to the absence of crack closure. Therefore, in

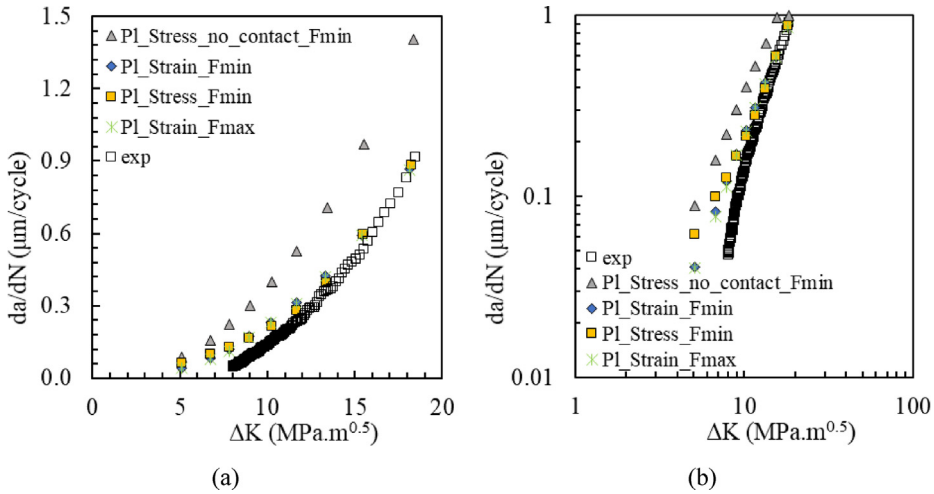

Fig. 11. Effect of physical parameter, stress state, and numerical parameter, instant of crack propagation, in *da/dN* versus *ΔK* curves, R = 0.1: (a) linear scales; (b) logarithmic scales.

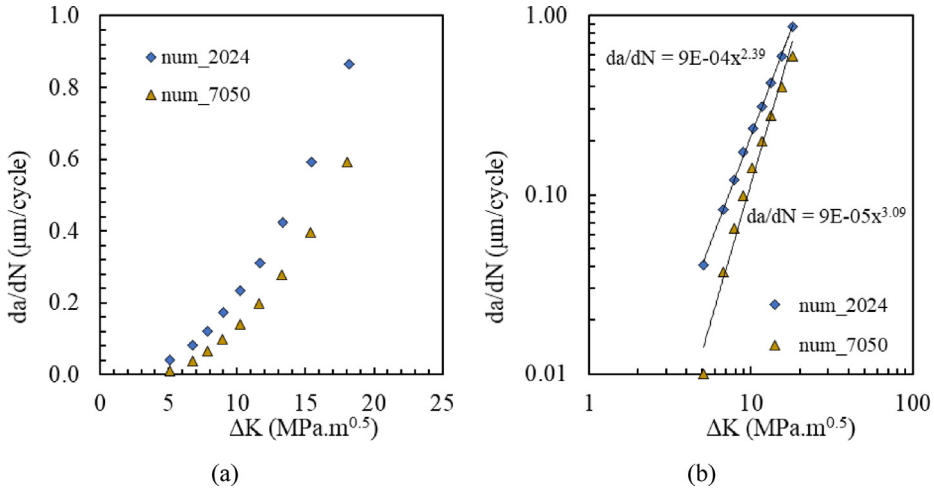

Fig. 12. Comparison of FCG rates of the aluminium alloys 2024-T351 and 7050-T6 (a) linear scales; (b) logarithmic scales; (plane strain; R = 0.1; $\Delta\varepsilon^p$ = 110%).

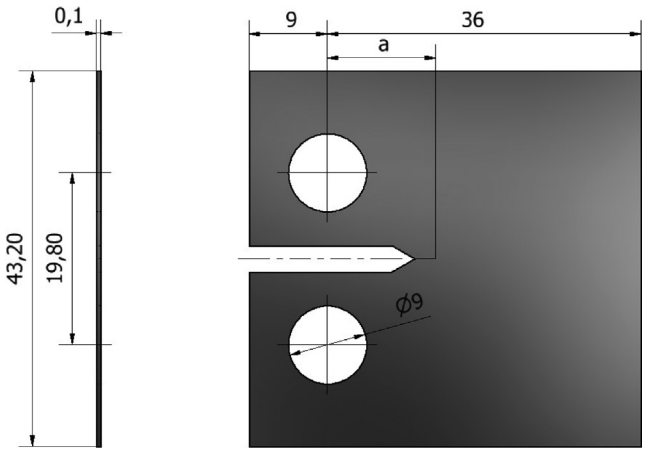

Fig. 13. Dimensions (mm) of the compact tension specimen.

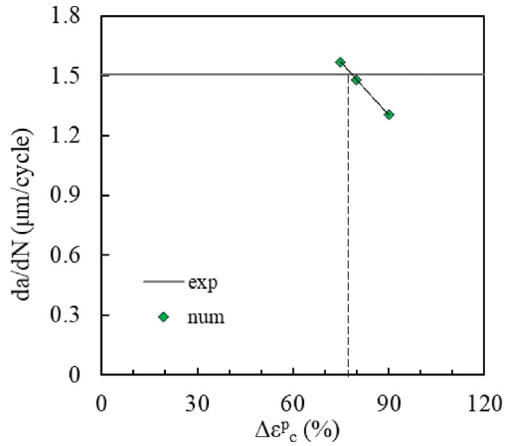

Fig. 14. Extraction of $\Delta\varepsilon_c^p$ for a_o = 24 mm, R = 0.1 and plane stress state (steel 18Ni300).

materials with a limited effect of stress ratio, cyclic plastic deformation may be expected to be the mechanism controlling FCG.

5. Conclusions

Fatigue crack growth was simulated here by node release when the accumulated plastic strain reaches a critical value. The main conclusions are:

- The numerical procedure was found to be very robust, showing a fast stabilization and independence relatively to the load level considered for node release.
- The accumulation of strain during one load cycle was detailed studied and compared with the variation of CTOD. A perfect similarity was observed between the evolution of accumulated plastic strain and plastic CTOD, which indicates that different parameters can be used to quantify crack tip plastic deformation.
- A critical plastic strain of 110% was obtained for the 2024-T315 aluminium alloy, comparing the experimental value of da/dN with numerical predictions obtained for a crack length of 26.5 mm, a stress ratio of 0.1 and plane strain state. This critical value was used to predict da/dN for different crack lengths and stress ratios.
- The predicted da/dN-ΔK curve was found to be linear in log-log scales with a slope m = 2.4, which is lower than the slope m = 3.6 presented by the experimental results. The difference is attributed to mechanisms like coalescence of microvoids or brittle mechanisms activated at relatively high loads.
- The variation of stress ratio and stress state did not affect the da/dN-ΔK curves, which indicate that the effect of these parameters is not directly linked with crack tip plastic deformation.
- Plasticity induced crack closure was found to be relevant only for plane stress state.
- FCG rate was also predicted for the 7050-T6 aluminium alloy and the 18Ni300 maraging steel. The predicted slopes of da/dN-ΔK curves ranged between 2.4 and 3.1 for the three materials studied. The predictions obtained for the steel agreed well with experimental results. In this material, the effect of stress ratio and specimen thickness on FCG rate is very limited. Therefore, the mechanisms causing the difference between numerical predictions and experimental results of AA2024-T351 may also explain the effect of stress ratio.

CRediT authorship contribution statement

M.F. Borges: Investigation, Formal analysis, Writing - original draft. **D.M. Neto:** Methodology, Software, Writing - review & editing. **F.V. Antunes:** Conceptualization, Supervision.

Declaration of Competing Interest

The authors declare that they have no known competing financial interests or personal relationships that could have appeared to

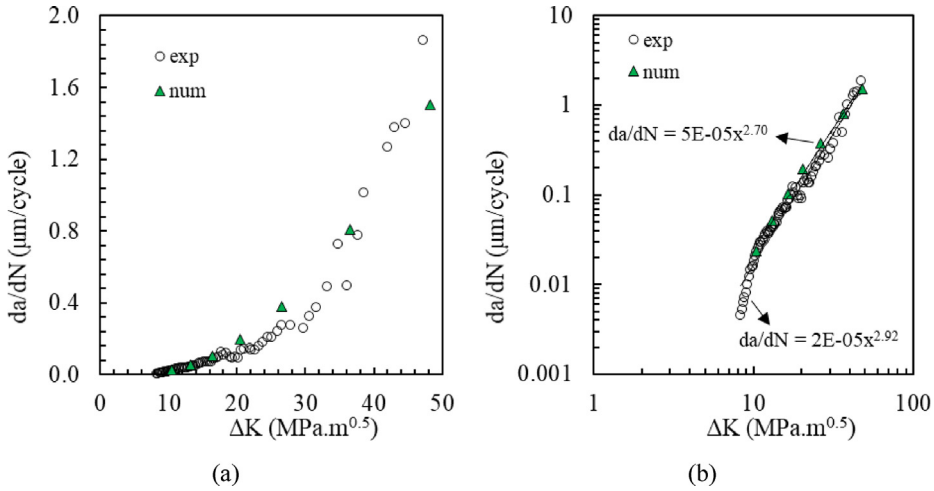

Fig. 15. Comparison of experimental and numerical FCG rates for 18Ni300 (a) linear scales; (b) logarithmic scales; (plane strain; R = 0.05; $\Delta\varepsilon^P$ = 78.6%).

influence the work reported in this paper.

Acknowledgements

The authors would like to acknowledge the sponsoring under the project no. 028789, financed by the European Regional Development Fund (FEDER), through the Portugal-2020 program (PT2020), under the Regional Operational Program of the Center (CENTRO-01-0145-FEDER-028789) and the Foundation for Science and Technology IP/MCTES through national funds (PIDDAC).

References

[1] ASTM E 647-11. Standard Test Method for Measurement of Fatigue Crack Growth Rates. Philadelphia: American Society for Testing and Materials (ASTM), 2011.
[2] ISO 12108, Metallic Materials – Fatigue Testing – Fatigue Crack Growth Method, Geneva: International Organization for Standardization (ISO), 2012.
[3] P.C. Paris, H. Tada, J.K. Donald, Service load fatigue damage — a historical perspective, Int. J. Fatigue 21 (1999) S35–S46.
[4] C.J. Christopher, M.N. James, E.A. Patterson, K.F. Tee, Towards a new model of crack tip stress fields, Int. J. Fract. 148 (2007) 361–371.
[5] W. Elber, Fatigue crack closure under cyclic tension, Eng. Fract. Mech. 2 (1970) 37–45.
[6] J. Tong, S. Alshammrei, B. Lin, T. Wigger, T. Marrow, Fatigue crack closure: a myth or a misconception? Fatigue Fract. Eng. Mater. Technol. 42 (12) (2019) 2747–2763.
[7] J. Pokluda, Dislocation-based model of plasticity and roughness-induced crack closure, Int. J. Fatigue 46 (2013) 35–40.
[8] J. Tong, L.G. Zhao, B. Lin, Ratchetting strain as a driving force for fatigue crack growth, Int. J. Fatigue 46 (2013) 49–57.
[9] J. Zhang, X.D. He, Y. Sha, S.Y. Dua, The compressive stress effect on fatigue crack growth under tension–compression loading, Int. J. Fatigue 32 (2010) 361–367.
[10] B. Ould Chikh, A. Imad, M. Benguediab, Influence of the cyclic plastic zone size on the propagation of the fatigue crack in case of 12NC6 steel, Comput. Mater. Sci. 43 (2008) 1010–1017.
[11] J.Z. Zhang, S.Y. Du, Elastic–plastic finite element analysis and experimental study of short and long fatigue crack growth, Eng. Fract. Mech. 69 (2001) 1591–1605.
[12] R.M. Pelloux, Crack extension by alternating shear, Eng. Fract. Mech. 1 (1970) 170–174.
[13] V. Tvergaard, On fatigue crack growth in ductile materials by crack–tip blunting, J. Mech. Phys. Solids 52 (2004) 2149–2166.
[14] R. Pippan, W. Grosinger, Fatigue crack closure: From LCF to small scale yielding, Int. J. Fatigue 46 (2013) 41–48.
[15] I. Gu, R.O. Ritchie, On the crack-tip blunting model for fatigue crack propagation in ductile materials, in: T.L. Sheppard, S.D. Panontin (Eds.), Fatigue and Fracture Mechanics, ASTM STP 1332, American Society for Testing and Materials, West Conshohocken, PA, 1999, pp. 552–564.
[16] F.V. Antunes, R. Branco, P.A. Prates, L. Borrego, Fatigue crack growth modelling based on CTOD for the 7050–T6 alloy, Fatigue Fract. Eng. Mater. Struct. 40 (2017) 1309–1320.
[17] J.M. Vasco-Olmo, F.A. Díaz, F.V. Antunes, M.N. James, Characterisation of fatigue crack growth using digital image correlation measurements of plastic CTOD, Theor. Appl. Fract. Mech. 101 (2019) 332–341.
[18] J.M. Vasco-Olmo, F.A. Díaz, F.V. Antunes, M.N. James, Plastic CTOD as fatigue crack growth characterising parameter in 2024–T3 and 7050–T6 aluminium alloys using DIC, Fatigue Fract. Eng. Mater. Struct. (2020) 1–12.
[19] M.F. Borges, F.V. Antunes, P.A. Prates, R. Branco, T. Vojtek, Effect of Young's modulus on Fatigue Crack Growth, Int. J. Fatigue 132 (2020) 105375.
[20] F.V. Antunes, M.S.C. Ferreira, R. Branco, P. Prates, C. Gardin, C. Sarrazin-Baudoux, Fatigue crack growth versus plastic CTOD in the 304L stainless steel, Eng. Fract. Mech. 214 (2019) 487–503.
[21] J.R. Rice, Mechanics of crack tip deformation and extension by fatigue. In: Grosskreutz, J. (Ed.), Fatigue Crack Propagation, ASTM STP 415. American Society for Testing and Materials, Philadelphia, PA, 1967, pp. 247–311.
[22] S.R. Bodner, D.L. Davidson, J. Lankford, A description of fatigue crack growth in terms of plastic work, Eng. Fract. Mech. 17 (2) (1983) 189–191.
[23] Y. Jiang, M. Feng, Modeling of fatigue crack propagation, J. Eng. Mater. Technol. 126 (1) (2004) 77–86.
[24] L. Susmel, The theory of critical distances: a review of its application in fatigue, Eng. Fract. Mech. 75 (2008) 1706–1724.
[25] Z.S. Hosseini, M. Dadfarnia, B.P. Somerday, P. Sofronis, R.O. Ritchie, On the theoretical modeling of fatigue crack growth, J. Mech. Phys. Solids 121 (2018) 341–362.
[26] L.F. Menezes, C. Teodosiu, Three-dimensional numerical simulation of the deep-drawing process using solid finite elements, J. Mater. Process. Technol. 97 (1-3) (2000) 100–106, https://doi.org/10.1016/S0924-0136(99)00345-3.
[27] M.C. Oliveira, J.L. Alves, L.F. Menezes, Algorithms and strategies for treatment of large deformation frictional contact in the numerical simulation of deep drawing process, Arch. Comput. Methods Eng. 15 (2008) 113–162.
[28] P. Alart, A. Curnier, A mixed formulation for frictional contact problems prone to Newton like solution methods, Comput. Methods Appl. Mech. Eng. 92 (1991) 353–375.
[29] B. Moreno, A. Martin, P. Lopez-Crespo, J. Zapatero, J. Dominguez, Estimations of fatigue life and variability under random loading in aluminum Al-2024T351 using strip yield models from NASGRO, Int. J. Fatigue 91 (2016) 414–422.
[30] T.J.R. Hughes, Generalization of selective integration procedures to anisotropic and nonlinear media, Int. J. Numer. Meth. Eng. 15 (1980) 1413–1418.
[31] H.R. Shercliff, N.A. Fleck, Effect of specimen geometry on fatigue crack growth in plane strain – II overload response, Fatigue Fract. Eng. Mater. Struct. 13 (3) (1990) 297–310.
[32] X. Zheng, H. Cui, X. Su, C.C. Engler-Pinto Jr., W. Wen, Numerical modeling of fatigue crack propagation based on the theory of critical distances, Eng. Fract. Mech. 114 (2013) 151–165.
[33] D. Kujawski, A fatigue crack driving force parameter with load ratio effects, Int. J. Fatigue 23 (2001) S239–S246.
[34] L. Llanes, Y. Torres, M. Anglada, On the fatigue crack growth behavior of WC-Co cemented carbides: kinetics description, microstructural effects and fatigue sensitivity, Acta Materialia 50 (9) (2002) 2381–2393.
[35] R. Pippan, C. Bichler, B. Tabernig, H. Weinhandl, Overloads in ductile and brittle materials, Fatigue Fract Eng. Mater. Struct. 28 (2005) 971–981.
[36] F.V. Antunes, L. Santos, C. Capela, J.M. Ferreira, J.D. Costa, J. Jesus, P. Prates, Fatigue crack growth in maraging steel obtained by selective laser melting, Appl. Sci. 9 (2019) 4412.